**ARTICLE**

# Multi-Bandgap Monolithic Metal Nanowire Percolation Network Sensor Integration by Reversible Selective Laser-Induced Redox

Junhyuk Bang[1], Yeongju Jung[1], Hyungjun Kim[2], Dongkwan Kim[1], Maenghyo Cho[2], Seung Hwan Ko[1,3] ✉

## HIGHLIGHTS

- A three single-phase Cu, $Cu_2O$, and CuO monolithic nanowire network was successfully fabricated by reversible selective laser-induced redox (rSLIR)

- Monolithic metal–semiconductor–metal multispectral photodetectors with Cu nanowire (CuNW) as an electrode and $Cu_2$ONW/CuONW having different bandgaps were suggested.

**ABSTRACT** Active electronics are usually composed of semiconductor and metal electrodes which are connected by multiple vacuum deposition steps and photolithography patterning. However, the presence of interface of dissimilar material between semiconductor and metal electrode makes various problems in electrical contacts and mechanical failure. The ideal electronics should not have defective interfaces of dissimilar materials. In this study, we developed a novel method to fabricate active electronic components in a monolithic seamless fashion where both metal and semiconductor can be prepared from the same monolith material without creating a semiconductor–metal interface by reversible selective laser-induced redox (rSLIR) method. Furthermore,



**rSLIR (reversible Selective Laser Induced Redox)**

rSLIR can control the oxidation state of transition metal (Cu) to yield semiconductors with two different bandgap states ($Cu_2O$ and CuO with bandgaps of 2.1 and 1.2 eV, respectively), which may allow multifunctional sensors with multiple bandgaps from the same materials. This novel method enables the seamless integration of single-phase Cu, $Cu_2O$, and CuO, simultaneously while allowing reversible, selective conversion between oxidation states by simply shining laser light. Moreover, we fabricated a flexible monolithic metal–semiconductor–metal multispectral photodetector that can detect multiple wavelengths. The unique monolithic characteristics of rSLIR process can provide next-generation electronics fabrication method overcoming the limitation of conventional photolithography methods.

**KEYWORDS** Monolithic integration; Seamless interface; Multi-bandgap nanowire; Laser-induced redox; Multispectral photodetector
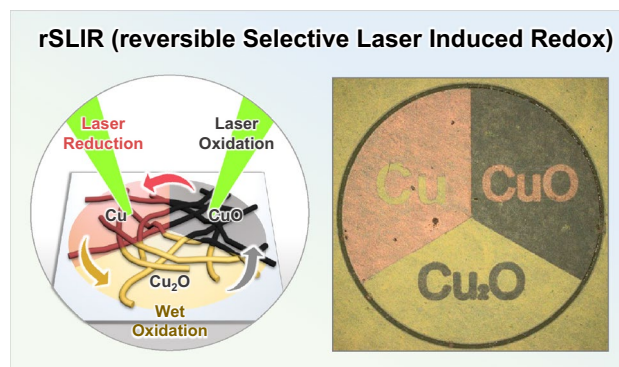
✉ Seung Hwan Ko, maxko@snu.ac.kr

1 Applied Nano and Thermal Science Lab, Department of Mechanical Engineering, Seoul National University, 1 Gwanak-ro, Gwanak-gu, Seoul 151-742, Republic of Korea

2 Department of Mechanical Engineering, Seoul National University, 1 Gwanak-ro, Gwanak-gu, Seoul 08826, Republic of Korea

3 Institute of Advanced Machines and Design, Institute of Engineering Research, Seoul National University, Seoul 08826, Republic of Korea

# 1 Introduction

Changing and controlling electrical properties as desired are crucial for the manufacturing of electronic devices. Transition metals with incompletely filled $d$-orbitals show variable oxidation states: different states form depending on oxidation conditions and different characteristics present [1]. Transition metal oxides have achieved complex functionality and high performance in diverse fields such as sensors [2, 3], memory devices [4, 5], and energy devices [6, 7]. Nevertheless, sophisticated arrangements and integration of multiple oxidation states are some of the challenges left unconquered.

Copper, an essential electronic material in nanotechnology, is found in a metallic state and two distinct stoichiometric oxidation states in nature: Cu (zero valent), $Cu_2O$ (monovalent), and CuO (bivalent). Cu has been intensively investigated for their high electrical conductivity and abundant reserves. As p-type semiconductors, $Cu_2O$ and CuO have bandgaps of 2.1 and 1.2 eV [8, 9]. $Cu_2O$ and CuO are also utilized in a broad range of applications, such as sensors [10, 11], energy devices [12, 13], chemical catalysts [14, 15], photocatalysts [16, 17], and biomedical devices [18, 19]. One-dimensional copper nanowire (CuNW) with a high aspect ratio has attracted attention due to its inherent electric and mechanical characteristics [20, 21]. However, because of its high surface-to-volume ratio, nanowires are more readily degraded than bulk metal, more sophisticated oxidation conditions require investigation to manipulate single-phase $Cu_2O$ or CuO.

The laser process allows on-demand control of the oxidation state of transition metals, in contrast with conventional thermal oxidation, which is unavailable to elaborate patterns of multiple oxidation states entirely due to heat spreads. The focused laser illumination generates localized heat and exceeds the critical reaction temperature very quickly. Therefore, photothermochemical reaction enables another oxidation state that exhibits different electrical properties with seamless interfacing [22–29]. However, previous technologies are still limited to 0 D nanoparticle or incomplete three-phase control. They also have not been used for independent patterning of Cu, $Cu_2O$, and CuO to nanowire networks.

This work presents reversible, selective laser-induced redox (rSLIR) of a three-single phase Cu, $Cu_2O$, and CuO monolithic nanowire network. We achieved three materials patterning, including one metal and two metal oxides. rSLIR combines the three processes that cross over the oxidation state of Cu-based nanowires; it is simple yet allows complex materials patterns. The prepared CuNW network was oxidized under low temperature and high humidity, transforming it into $Cu_2ONW$ networks. Afterward, laser irradiation of the $Cu_2ONW$ network selectively induced oxidation or reduction, obtaining a monolithic, seamless CuNW, $Cu_2ONW$, and CuONW network. rSLIR constituted a 3-phase cycle from synthesized CuNW to wet-oxidized $Cu_2ONW$, laser-oxidized CuONW, and laser-reduced CuNW. The 3-phase cycle did not restrict the starting state of the nanowire network during rSLIR. We demonstrated that rSLIR could be conducted on nanowire networks in which Cu and $Cu_xO$ are irregularly mixed, assuring their reversibility. Moreover, to verify that our method is suitable for multiple disparate electronic device fabrication, we suggested using an MSM (metal–semiconductor–metal) visible light photodetector with CuNW as an electrode and $Cu_2ONW$ and CuONW, having different bandgaps, in the visible light detecting channels.

# 2 Experimental Section

## 2.1 Synthesis of CuNW

Hydrothermal synthesis was implemented for CuNW. Copper (II) chloride dihydrate (Sigma-Aldrich, No. 467847) was the precursor, HDA (Sigma-Aldrich, No. 445312) was the ligand, and glucose (Sigma-Aldrich, No. 5767) was used as a reducing agent. 0.84 g of $CuCl_2$ and 5.2 g of HDA were dissolved in 400 mL of deionized water with vigorous stirring. Next, 2 g of glucose was added to the prepared solution and reacted at 100 °C for 7 h and 20 min. During the growth of nanowire, the color of the CuNW solution change to reddish-brown. Last, centrifugation for 15 min at 1500 rpm was performed with IPA several times to purify CuNW solution. The synthesized CuNW is 80–100 thick and 80–110 μm long and is highly conductive with a sheet resistance of 50 Ω $sq^{-1}$ at 89% transparency in Fig. S1.

## 2.2 Wet Oxidation to Produce Cu$_2$ONW

The CuNW network became a Cu$_2$ONW network through wet-oxidation with mild temperature conditions, as shown in Fig. S2. First, a uniform CuNW network was obtained through vacuum filtration. After that, the red CuNW network was initially oxidized for 12 h at 100 °C with high humidity. The sample turned dark red, and at this time, only a weak copper oxide peak was detected by XRD due to its insufficient oxide grain sizes. Next, the dark red Cu$_X$ONW network was oxidized in one day at room temperature, and high relative humidity (over 80%), turning from dark red to bright yellow, indicated a single oxidation state of Cu$_2$ONW.

## 2.3 DFT Calculations

Spin-polarized density functional theory (DFT) calculations were performed using density functional theory as implemented in the Vienna ab initio simulation package [30, 31], using the projector augmented wave with the Perdew–Burke–Ernzerhof generalized gradient approximation (GGA) exchange–correlation function [32–34]. An energy cutoff of 520 eV was used for all calculations. The valence configurations of the Cu and O elements are $3p^6 3d^{10} 4s^1$ and $2s^2 2p^4$, respectively. The Cu$_2$O(111) $(2 \times 1)$ slab was constructed based on the fully relaxed Cu$_2$O bulk unit cell, and the optimized O$_2$ molecule was positioned on the Cu$_2$O(111) substrate to make the interfacial nanostructure. Monkhorst–Pack $k$-point sets were used for all the calculations on the Cu$_2$O(111) $(2 \times 1)$ slab model, $1 \times 4 \times 1$. The climbing image nudged elastic band (CI-NEB) method was used with the limited-memory Broyden–Fletcher–Goldfarb–Shanno (L-BFGS) optimizer until the residual forces were below 0.05 eV Å$^{-1}$ to calculate the reaction barriers for Cu$_2$O oxidation [17, 35, 36]. The adsorption energy was computed to determine the energetically favorable O$_2$ molecule adsorption site on Cu$_2$O(111) surface following [37]:

$$E_{ads} = E_{O_2 - Cu_2O(111)_{surf}} - E_{O_2} - E_{Cu_2O(111)_{surf}} \tag{1}$$

where $E_{ads}$ is the adsorption energy and $E_{O_2 - Cu_2O(111)_{surf}}$, $E_{O_2}$, and $E_{Cu_2O(111)_{surf}}$ are the total energy of the O$_2$ molecule absorbed on the Cu$_2$O(111) surface, the O$_2$ molecule, and the bare Cu$_2$O(111) surface obtained from the first-principles calculations, respectively.

## 2.4 Finite Element Analysis

Finite element analysis was conducted to simulate homogenous photothermal effect during the laser oxidation process of Cu$_2$ONW (Comsol Multiphysics). In the simulation, highly percolated Cu$_2$ONW network locates on a SiO$_2$ substrate, and the laser beam illuminates on the Cu$_2$ONW perpendicularly from the top. According to the Cu$_2$ONW used in the experiments, a Cu$_2$ONW was modeled as a cylinder with a diameter of 100 nm and a length of 100 μm. Each Cu$_2$ONW was placed 2 μm apart, and the same arrangement was stacked by rotating 90 degrees to reflect the overlapping of Cu$_2$ONW. We also considered a Gaussian laser beam with a width of 20 μm and a power of 40 mW.

## 2.5 Characterization

Scanning electron microscope (SEM, MERLIN Compact), X-ray diffraction (XRD, D8 Advance, 2020), and Raman spectroscopy (Renishaw InVia Raman microscope) were used to characterize the morphology and composition according to the phase transition of CuNW, Cu$_2$ONW, and CuONW.

## 2.6 Fabrication of Flexible Photodetectors

In this study, a 532 nm visible light laser (Sprout-G-5W, Lighthouse Photonics, USA) and Galvano-mirror (hurrySCAN II, Scanlab, Germany) were used for laser patterning. Figure S3b describes the fabrication steps. (1) For the Cu–Cu$_2$O–Cu photodetector, spaced laser reduction hatch scanning produced CuNW electrodes with a Cu$_2$ONW detecting channel 30 μm wide. (2) For the Cu–CuO–Cu structure, a CuONW detecting channel was produced through laser oxidation, and then CuNW electrodes were accomplished through laser reduction. (3) Cu–Cu$_2$O&CuO–Cu, firstly, CuONW was fabricated by laser oxidation. After, laser ablation 40 separate CuONW and Cu$_2$ONW detecting channels with 40 μm width were formed. Next, CuNW electrodes were formed on both sides in the same way as above. Laser ablation of the photodetector surroundings prevented electrical interference associated with external Cu$_2$ONW. Next, to fabricate a flexible photodetector, polyurethane acrylate (PUA, SEA-1, CCTech) was

spin-coated on the photodetector at 500 rpm for 30 s. Last, the device was placed under a UV lamp for 120 s to cure the PUA, and the PUA-nanowire composite was obtained.

### 2.7 Photodetector Measurement Setup

The single-wavelength laser beams (450, 532, and 650 nm) were expanded to fully cover the photodetector channel. The expanded beam was adjusted through the nd filter for achieving intensities of 5, 10, and 15 mW cm$^{-2}$, and the photocurrent was measured.

## 3 Results and Discussion

### 3.1 Reversible Selective Laser-Induced Redox

The rSLIR schematic of the CuNW, Cu$_2$ONW, and CuONW network is shown in Fig. 1a The continuous-wave laser (532 nm wavelength) irradiated the Cu$_2$ONW networks (yellow color) fabricated through CuNW network wet oxidation. Laser-induced photothermal energy selectively generated oxidation or reduction according to the surroundings. Under ambient conditions, the photothermal energy led to selective oxidation, and CuONW (black color) developed. The laser enforced bonds between Cu$_2$ONW and its adjacent oxygens and created another oxidation state, CuONW. When reducing agents surrounded the Cu$_2$ONW network, the laser scan selectively reduced CuNW (red color). Ethylene glycol (EG), used for effective laser reduction, was dehydrated by photothermal energy, turning it into acetaldehyde, reducing the metal oxides [23, 38, 39].

rSLIR enables on-demand patterning of CuNW, Cu$_2$ONW, and CuONW with seamless interfacing. The microscopic optical images in Fig. 1b describe the step-by-step fabrication of the delicate three single-phase pattern. Before the consecutive laser oxidation and reduction, we prepared a non-patterned 2 mm diameter Cu$_2$ONW network disk through laser ablation (Fig. 1bi). Ten cycles of laser hatch scanning produced the black CuONW pattern (right circular arc and the letter of Cu$_2$O) (Fig. 1bii). Applying EG on the Cu$_2$ONW and CuONW pattern afterwards achieved a reddish CuNW pattern (left circular arc and the letter of CuO) with laser hatch scanning (Fig. 1biii). Last, the remnant EG was removed with ethanol. rSLIR usage can also be expanded to a large-scale pattern. A red-yellow-black (Cu, Cu$_2$O, and CuO, respectively) tartan check pattern was manufactured through laser oxidation and reduction as 2 cm × 2 cm square Cu$_2$ONW networks (Fig. 1ci, ii). Furthermore, rSLIR can be extended to the elastomeric stretchable substrate (Fig. S4).

During conventional thermal oxidation to form individual Cu$_2$O and CuO, the high temperature and partial pressure of oxygen should be controlled [40]. Additionally, CuO is usually created after forming the Cu$_2$O layer [41]. Likewise, during laser oxidation of Cu, incidental Cu$_2$O is simultaneously formed at the edge of CuO and affected by the heat spreading. However, the wet oxidation for Cu$_2$ONW before the laser process contributed to forming the single-phase pattern. The novel CuNW, Cu$_2$ONW, and CuONW patterning process gave clear advantages over previous processes, including (1) a monolithic, seamless interface between individual oxidation state, (2) mask-less in-situ process, and (3) low-temperature and ambient conditions process.

### 3.2 rSLIR for Monolithic CuNW, Cu$_2$ONW, and CuONW Network

In general, laser scanning fills the desired area through hatch scanning so that the pattern width is the practical and essential parameter. The laser power determined the amount of generated heat and affected the phase change width. Figure 2a shows the CuNW linewidth resulting from laser reduction by varying the laser intensity. The minimum resolution was obtained at 26 mW, and 10 mm s$^{-1}$, and the power density was 67.6 Kw cm$^{-2}$ (Fig. S5a). As the laser power increased, the width thickened, and excessive power produced a damaged pattern (Fig. S6a). Thus, to enlarge the pattern width without damage, the laser beam must be defocused like in the inset schematic in Fig. 2a. Figure 2b shows the available pattern width of CuONW through laser oxidation based on a ten-cycle laser scan. Laser oxidation obtains the narrowest line under the condition of 4 mW power, 1 mm s$^{-1}$ scanning speed, and the power density at this time is 10.4 kW cm$^{-2}$. (Fig. S5b) The nanowires melt and become damaged at high intensity, and the defocused beam achieves a thicker width line, as found earlier (Fig. S6b). In this regard, since laser beam size dominantly affects the pattern width, if the beam size can be further narrowed, the pattern width is likely to decrease.
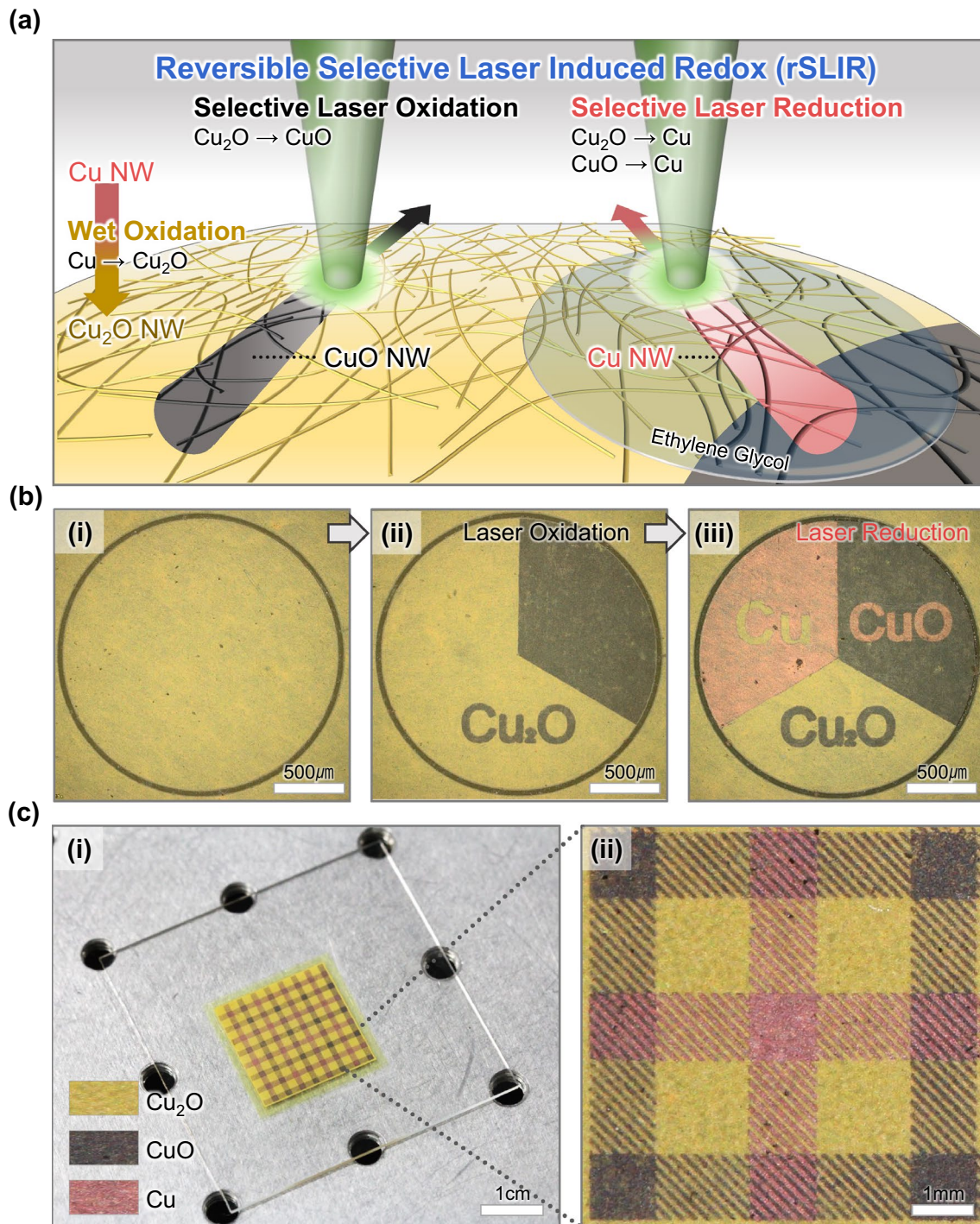
**Fig. 1** **a** Schematic of reversible selective laser-induced redox (rSLIR) for the monolithic CuNW, $Cu_2ONW$, and CuONW network. **b** Optical microscopy image depicting the flow of rSLIR for **i** $Cu_2ONW$ **ii** $Cu_2O$, and CuO patterns obtained after laser oxidation with 25 mW of power and a 1 mm s$^{-1}$ scanning speed. **iii** Cu, $Cu_2O$, CuO pattern obtained after laser reduction (scale bar: 500 µm). **c** Optical image of the sophisticated three-coloration pattern, **i** tartan check pattern (scale bar: 1 cm), **ii** magnified image of the tartan check pattern. The black CuONW and the red CuNW patterns were fabricated under ten cycles of the hatch scan at 125 mW power and 10 mm s$^{-1}$ scan speed, and one cycle of the hatch scan at 125 mW power and 10 mm s$^{-1}$ scan speed, respectively (scale bar: 1 mm)
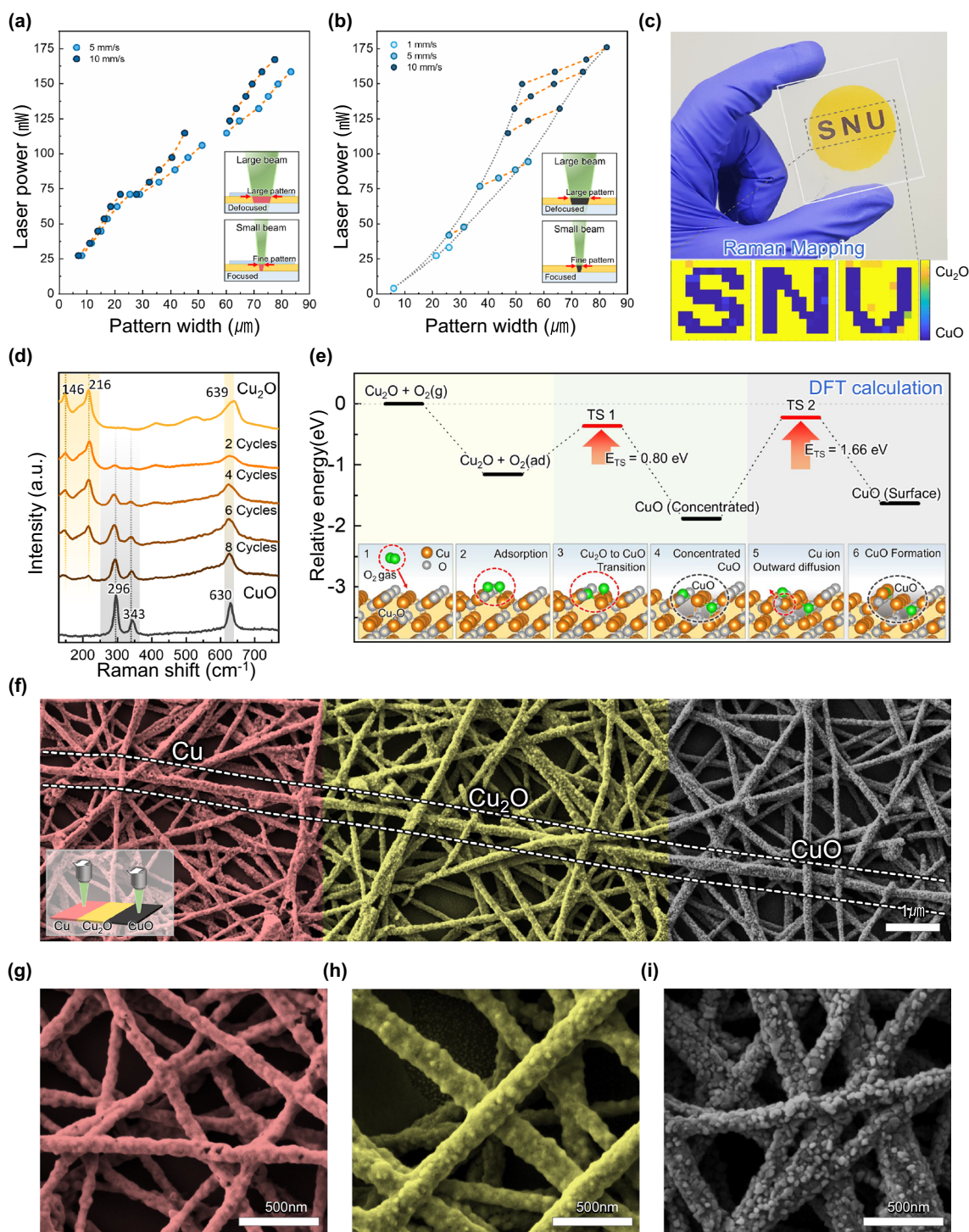
**Fig. 2** **a** An increase in laser-reduced CuNW pattern width according to laser power. **b** An increase in laser-oxidized CuONW pattern width according to laser power. **c** Optical image of Cu$_2$ONW, CuONW pattern, and quantitative Raman mapping image investigated by 121 points data at 1 mm intervals (scale bar: 500 cm). **d** Raman spectroscopy of laser oxidation at different scan cycles at 125 mW power and 10 mm s$^{-1}$ scanning speed. **e** DFT model for theoretical investigation of Cu$_2$O to CuO transition. The six inset schematics depict the oxygen and copper atoms move as oxidation proceeds. **f** SEM image of monolithic CuNW, Cu$_2$ONW, and CuONW network, the left red area Cu, central area Cu$_2$O, and right area CuO. The inset schematic describes the process for making a monolithic structure (scale bar: 1 μm). **g** SEM image of CuNW. **h** SEM image of Cu$_2$ONW. **i** SEM image of CuONW (scale bar: 500 nm)

Quantitative analysis of laser oxidation was completed using XRD and Raman spectroscopy. XRD analysis verified that wet-oxidized Cu$_2$ONW, laser-oxidized CuONW, and laser reduced CuNW were single-phase (Fig. S7). To evaluate the crystallinity of the materials, we calculate the full width at half maximum (FWHM) of the X-ray diffraction line of both CuONW and Cu$_2$ONW in Table S1. Generally, the sharper the XRD peak, the better crystallinity materials have. Considering that the sharpness of the XRD peak and FWHM value have inverse proportion, the results indicate that CuONW has better crystallinity compared to Cu$_2$ONW.

Raman spectroscopy is an excellent way to identify different oxide compositions and confirm the atomic arrangements of materials. Through surface-sensitive Raman analysis, it can be seen that oxidation occurs on the surface of the nanowire. Other XRD accurately detects when grains grow sufficiently, this Raman spectroscopy detects amorphous crystals proving that Cu$_2$ONW and CuONW have single phases. According to the laser scan cycle for oxidation from Cu$_2$O to CuO, the Raman peak change is analyzed in Fig. 2d. The spectrum clarifies the oxidation state change from Cu$_2$ONW to CuONW. The initial Cu$_2$ONW spectrum consists of 5 peaks (three intense peaks at 146, 216, and 639 cm$^{-1}$, and two weak peaks at 415 and 529 cm$^{-1}$). As the laser cycles were incremented, the Cu$_2$O peaks (146 and 216 cm$^{-1}$) gradually disappear, and simultaneously the CuO peaks (296 and 343 cm$^{-1}$) increase. Eventually, after ten cycles of laser scanning, only the CuO peaks remain and the laser-oxidized CuONW does not possess Cu$_2$ONW.

Raman mapping investigated the reliability of the Cu$_2$ONW and CuONW pattern, shown in Fig. 2c. The ratio of the most intense peak of Cu$_2$O (216 cm$^{-1}$) and CuO (296 cm$^{-1}$) validates that the CuO pattern was uniformly generated even on a large scale by laser oxidation. Also, in Fig. S8, the Raman spectrum at different points shows the high repeatability of rSLIR.

The laser scanning process was simulated using finite element analysis in Fig. 2e to thoroughly understand the Cu$_2$ONW and Cu$_2$ONW laser-induced oxidation. Figure S9 shows that the area exposed to the laser was heated, while the remaining area was at room temperature, indicating that the laser selectively raises the energy of the exposed area. Considering the energy provided by laser scanning, the Cu$_2$O oxidation procedure was inspected by the first-principles calculations in detail. The first-principles calculations were conducted on the energetically

most stable Cu$_2$O (111) surface model (Fig. S9 and Table S2) with a free O$_2$ molecule on it. All possible O$_2$ adsorption sites on the Cu$_2$O (111) surface (Fig. S10 and Table S3) were examined, and the energetically stable site was considered in all following calculations to explore the potential adsorption sites. Figure 2e inset 2 shows an O$_2$ molecule adsorbs on a bridge site of copper atoms. The adsorbed O$_2$ molecule then interacts with neighboring copper atoms to dissociate into two oxygen atoms and oxidize the periphery, as shown in the Fig. 2e inset 2–4. For further oxidation inside Cu$_2$ONW, an oxygen atom moves inward, or a copper atom diffuses outward. Notably, it requires relatively lower energy for a copper atom inside the bulk to diffuse outward than the energy for the oxygen atom to go inside, so it is preferential for a copper atom to diffuse to the Cu$_2$ONW surface for further oxidation [42]. Figure 2e inset 4–6 shows a copper atom inside the bulk Cu$_2$ONW diffuses out to the surface and balances the copper concentration. The Cu$_2$ONW oxidation process could be classified into two steps: (1) adsorption and dissociation of an oxygen molecule and (2) the diffusion of a copper atom toward the surface. For each step, the calculated activation energy barrier was 0.80 eV (TS1) and 1.66 eV (TS2), so that during the second step, the copper atom diffusion outward was the rate-determining step for Cu$_2$ONW oxidation. The reaction for the rate-determining step requires relatively high activation energy and occurs inside the bulk. It is essential to deliver an appropriate amount of energy and expose it in a certain amount of time for proper oxidation. Therefore, laser oxidation was only possible with a continuous laser (Fig. S11). Incidentally, considering that the copper atoms diffuse from bulk to the Cu$_2$O surface, the surface roughness increases, and the width of Cu$_2$ONW thickens during oxidation.

In Fig. 2f, the SEM image of the seamless CuNW, Cu$_2$ONW, and CuONW network demonstrates the morphology transmutation mentioned above. The inset image in Fig. 2f depicts a process diagram to fabricate a network parallelly arranged in three phases, where the left side red pseudocolor area is laser reduced CuNW, the middle yellow pseudocolor is Cu$_2$ONW, and the right side black pseudocolor is laser-oxidized CuONW. The dotted line presents a nanowire including three phases Cu, Cu$_2$O, and CuO simultaneously. This nanowire proves that CuONW is rougher and thicker than Cu$_2$ONW. Figure 2g–i exhibits the magnified SEM image of CuNW, Cu$_2$ONW, and CuONW, depicting

surface roughness and thickness changes. The diameter increases to 120–150 nm during wet oxidation to become $Cu_2ONW$. Then, through laser oxidation, the diameter of CuONW becomes 130–170 nm. CuNW becomes 80–110 nm again. Unlike the oxidation state, CuNW has a thinner nanowire thickness and low roughness. Furthermore, the nanowire network did not break using rSLIR, maintaining seamless interfacing remains even though the phase transition of synthesized CuNW occurred repeatedly.

### 3.3 Reversible Oxidation State Control by rSLIR

rSLIR consists of wet oxidation, laser oxidation, and laser reduction and shows circularity when linking each process's reactive and produced substances. Figure 3a shows that Cu can go back to its original oxidation state: $Cu \rightarrow Cu_2O \rightarrow CuO \rightarrow Cu$ during rSLIR. Because of its unique properties, rSLIR ensures a high degree of freedom on the process sequence to fabricate a specific pattern. Any state in which Cu, $Cu_2O$, and CuO single-phase and multi-phase coexist changes into the desired oxidation state. Figure 3b presents rSLIR to a $Cu_XONW$ network. The dark-reddish $Cu_xONW$ network is prepared by degradation at 200 °C for 30 min. According to the following process, the $Cu_XONW$ network is sequentially transformed into a single-phase CuNW, $Cu_2ONW$, and CuONW network: (1) Laser reduction changed the $Cu_XONW$ network to a red CuNW network. (2) The CuNW network was converted to
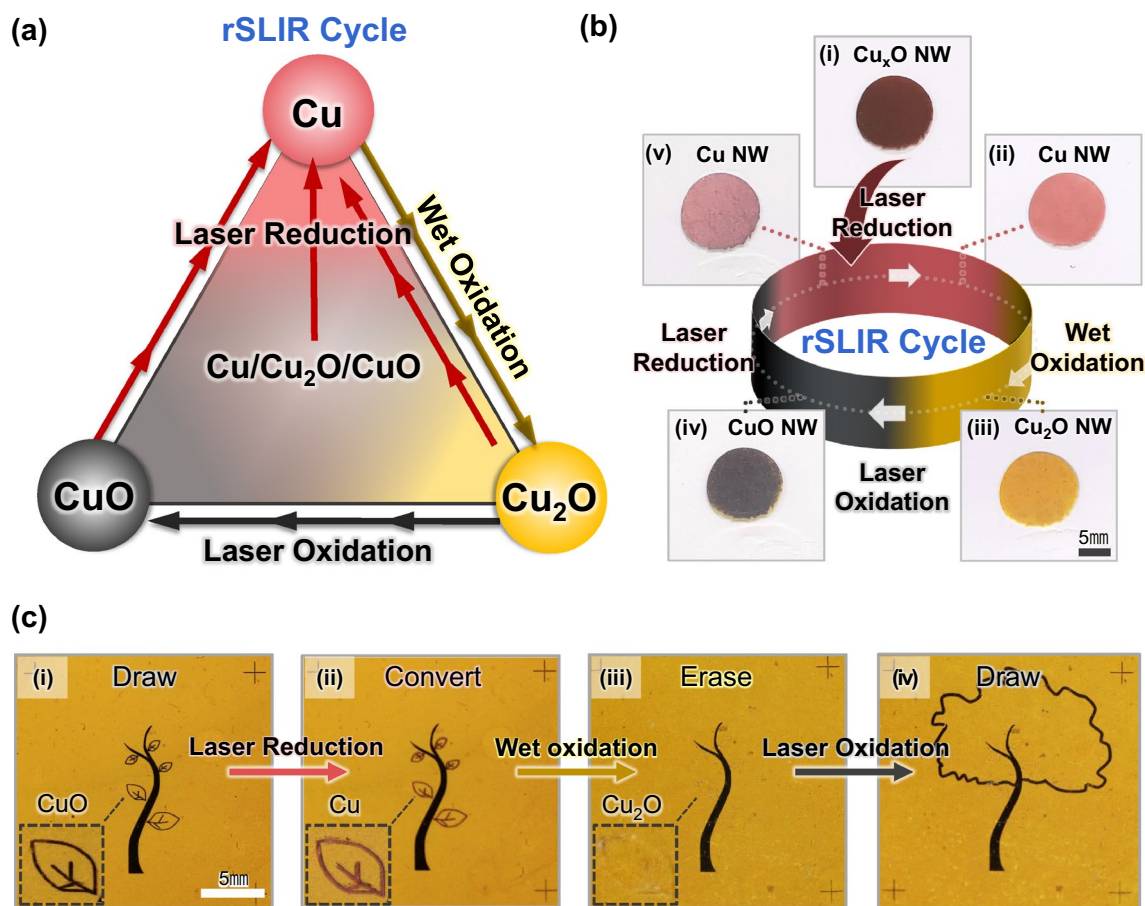


**Fig. 3 a** A process diagram of rSLIR cycle; the arrows connect the reactive substance and the produced substance. **b** An optical image of rSLIR on the $Cu_xONW$ network. **i** Prepared CuxONW network oxidized at 200 °C for 30 min. **ii** The first laser reduced CuNW. **iii** Wet-oxidized $Cu_2ONW$. **iv** Laser-oxidized CuONW. **v** The second laser-reduced CuNW (laser oxidation, laser reduction conditions: 125 mW, 10 mm s$^{-1}$, scale bar: 5 mm). **c** An optical image of rSLIR on the prepared pattern. **i** Yellow $Cu_2ONW$ with black CuONW tree pattern, and the inset optical image is a magnified black CuONW leaf. **ii** The leaves are converted to red CuNW through laser reduction. **iii** Removal of the pattern by wet oxidation. **iv** The new pattern is added to the existing pattern through laser oxidation (laser oxidation, laser reduction conditions: 125 mW, 10 mm s$^{-1}$, scale bar: 5 mm)

yellow Cu$_2$ONW through wet oxidation and (3) became a black CuONW network by laser oxidation. (4) It returned to CuNW after going through laser reduction again.

Furthermore, customized re-writing is available by rSLIR. Figure 3c shows the seriate re-writing process, leaving the tree trunk intact, erasing only the leaves, and getting a new leafy pattern through the following steps: (1) Laser reduction converted the CuONW leaves pattern into CuNW. (2) The reduced CuNW became Cu$_2$ONW by wet oxidation, which was identical to the yellow background. Since the wet oxidation was conducted under low temperature (100 °C), only CuNW suffered phase conversion to Cu$_2$ONW. The remaining Cu$_2$ONW and CuONW did not undergo a phase change during wet oxidation and maintained their color. (3) After that, laser oxidation fabricated a new black CuO pattern.

CuNW is susceptible to oxidation under ambient conditions due to its high surface-volume ratio, forming an irregular oxide layer and losing conductivity. For this reason, the reduction of nanomaterials has been a critical issue. Therefore, rSLIR employing circularity of the individual oxidation states will resolve the obstacle for broadening the uses for copper-based nanowire electronics. Furthermore, our method allows electrical property control through the crossover of copper oxidation states, restores its conductivity, and functionalizes through oxidation state transition.

### 3.4 Multispectral Photodetector Integration

The visible light photodetector is a foundational optoelectronic device. Moreover, its simple metal–metal oxide–metal (MSM) structure can replace the stacked-layer photodetector. Since the threshold of the light wavelength for generating a photocurrent is determined according to the bandgap of metal oxide, it is possible to easily fabricate visible-light photodetectors gaining a different wavelength threshold using multi-bandgap Cu$_2$ONW and CuONW detecting channels with different bandgaps. In particular, illuminating with low energy red (650 nm, 1.9 eV) light excites electrons in CuO alone and has a relatively low bandgap. However, green (532 nm, 2.3 eV) and blue (450 nm, 2.8 eV) lights excite electrons in CuO and Cu$_2$O. Here, we fabricated three types of photodetectors with varying responses according to wavelength and intensity through rSLIR.

Figure 4a illustrates the schematic of the three visible-light photodetectors, Cu–Cu$_2$O–Cu, Cu–CuO–Cu, and Cu–Cu$_2$O&CuO–Cu, fabricated by rSLIR. The Cu–Cu$_2$O–Cu and Cu–CuO–Cu photodetectors consist of a single oxidation state detecting material, and their dimensions are 30 μm with a 2 mm height. Cu–Cu$_2$O&CuO–Cu contains 40 parallel Cu$_2$O and CuO channels with a width of 30 μm and a height of 50 μm. Moreover, we manufactured flexible photodetectors using simple polyurethane acrylate (PUA) embedded and detached from the glass substrate in Fig. 4b [43, 44]. These photodetectors show high oxidation-resistant property and bending durability (Fig. S12).

The behavior of the three types of photodetectors was confirmed by measuring the photocurrent response to red (650 nm, 1.9 eV), green (532 nm, 2.3 eV), and blue light (450 nm, 2.8 eV), and the moderate light intensity (5, 10, and 15 mW cm$^{-2}$) under 5 V bias voltage, shown in Fig. S13. Usually, light illumination generates a photocurrent, and the photocurrent gradually rises and decays when the light is turned on or off.

The bi-exponential relaxation equation containing the fast ($A_1$, $\tau_1$) and slow parts ($A_2$, $\tau_2$) was used to analyze the gradual rise and decay curves for a quantitative approach.

$$I = I_0 + A_1\left(1 - \exp\left(-t/\tau_1\right)\right) + A_2\left(1 - \exp\left(-t/\tau_2\right)\right) \quad (2)$$

The relaxation time constant ($\tau_1$, $\tau_2$) represents the curve shape, and the inset schematic depicts fast and slow relaxation. The quantitative analysis of the bi-exponential equation fitting shows a clear tendency for the illuminated light wavelength. Figure 4c shows the photocurrent curves divided into the rise and decay and the relaxation constants according to the red (650 nm, 1.9 eV), green (532 nm, 2.3 eV), and blue light (450 nm, 2.8 eV) illumination of each photodetector with 10 mW cm$^{-2}$ intensity. The rise and decay constants of the Cu–Cu$_2$O–Cu photodetector were estimated to be $\tau_{r1} = 0.25$ s, $\tau_{r2} = 5.4$ s, $\tau_{d1} = 0.7$ s, and $\tau_{d2} = 11.3$ s in green, $\tau_{r1} = 0.26$ s, $\tau_{r2} = 5.4$ s, $\tau_{d1} = 0.7$ s, and $\tau_{d2} = 11.3$ s in blue. The rise, decay constants for Cu–CuO–Cu are $\tau_{r1} = 0.10$ s, $\tau_{r2} = 7.4$ s, $\tau_{d1} = 0.12$ s, and $\tau_{d2} = 8.5$ s in red, $\tau_{r1} = 0.11$ s, $\tau_{r2} = 7.6$ s, $\tau_{d1} = 0.11$ s, and $\tau_{d2} = 9.0$ s in green, $\tau_{r1} = 0.11$ s, $\tau_{r2} = 7.2$ s, $\tau_{d1} = 0.13$ s, and $\tau_{d2} = 8.4$ s in blue. In these two types, the time constants barely changed regardless of the light wavelength. This consistency proceeds from the material's inherent electron trap time, where the photon energy according to the wavelength has a minimal effect [45]. On the contrary, the time constants shift for the
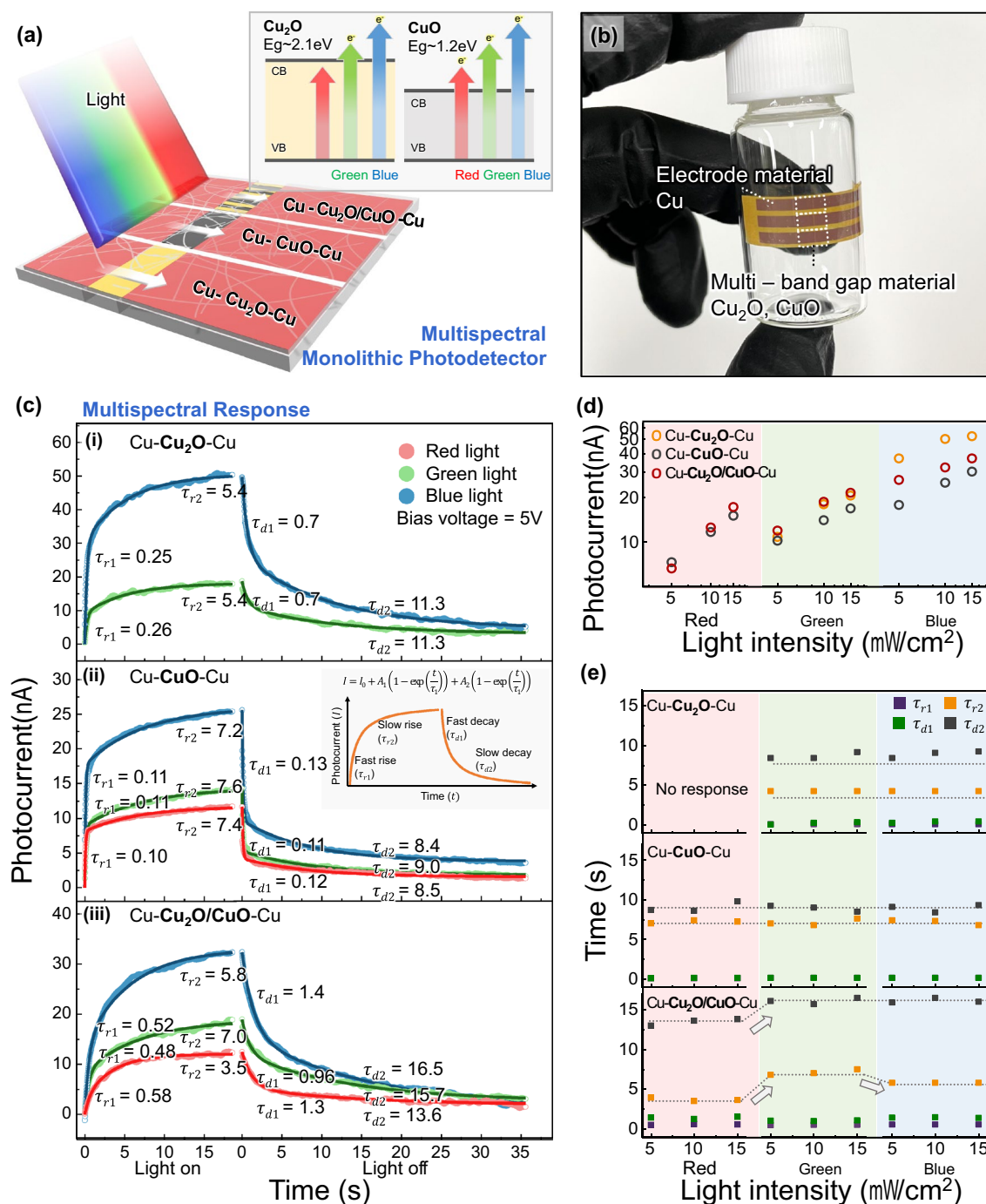
**Fig. 4 a** The schematic depicts monolithic integration for multispectral photodetectors. The schematic shows the different wavelength thresholds caused by the bandgap difference between $Cu_2O$ and $CuO$. **b** PUA-nanowire composite flexible photodetector: red color CuNW as electrode region, and a detecting channel between the two electrodes. **c** Photocurrent and time constant according to 10 mW cm$^{-2}$ light on or off, the inset schematic presents fast and slow relaxation constants of bi-exponential relaxation. **i** The Cu–$Cu_2O$–Cu photodetector. **ii** Cu–CuO–Cu photodetector. **iii** Cu–$Cu_2O$&CuO–Cu photodetector. **d** Log scale plot of the photocurrent magnitude at intensities of 5, 10, and 15 mW cm$^{-2}$ for red (650 nm wavelength), green (532 nm wavelength), and blue light (450 nm wavelength). **e** Rise and decay constants at intensities of 5, 10, and 15 mW cm$^{-2}$ for red (650 nm wavelength), green (532 nm wavelength), and blue light (450 nm wavelength)

Cu–Cu$_2$O&CuO–Cu photodetector since the Cu$_2$O and CuO produce different signals.

In addition, to verify that this tendency was preserved with changes in luminous light intensity, we investigated the photocurrent magnitude and the time constants on all occasions. Figure 4d presents the photocurrent dependence on the light wavelength and intensity. As the light intensity increased, the photocurrent increased linearly on a log scale. The shorter the wavelength, the higher the photocurrent, even with the same intensity. As mentioned earlier, the bandgap of Cu$_2$O is higher than red light photon energy, and only the Cu–Cu$_2$O–Cu photodetector did not respond to red light in this range, yet it generated more photocurrent than other samples under green and blue light.

Figure 4e is the rise and decay constants according to wavelength and intensity. We demonstrated that the time constants of the Cu–Cu$_2$O–Cu and Cu–CuO–Cu photodetectors remained nearly fixed while varying the wavelength and the power. This consistency means that a detecting channel with a single material requires additional measurement for the independent determination of wavelength and intensity. The time constants for the Cu–Cu$_2$O&CuO–Cu photodetector, consisting of two detecting materials, shifted by wavelength, not intensity. Hence, this photodetector could be used to confirm the wavelength and intensity of the incident light by estimating the time constants and magnitude.

## 4 Conclusion

We presented rSLIR as the first technology to obtain a monolithic CuNW, Cu$_2$ONW, and CuONW network with a seamless interface. The conventional thermal oxidation method hinders selective patterning due to heat spreading, and it is incompatible with heat-susceptive substrates. Apart from other methods, our work achieved mask-less in situ oxidation state control under low temperature and ambient conditions. Moreover, this method induces the desired oxidation state regardless of the original state, restoring conductivity or imparting functionality. Experimental and theoretical analyses verified patterning performance and the Cu$_2$O to CuO oxidation mechanism. A single nanowire with triple oxidation states indicates that rSLIR is a promising substitute for photolithography. Finally, rSLIR can be used to fabricate visible light photodetectors that generate varying photocurrents in accordance with wavelength and intensity. In this respect, our method works for controlling the electrical properties of transition metals. Thus we expect this technology to be exploited in various thin-film electronic devices.

## References

1. Y. Tokura, N. Nagaosa, Orbital physics in transition-metal oxides. Science **288**(5465), 462–468 (2000). https://doi.org/10.1126/science.288.5465.462

2. E. Lee, Y.S. Yoon, D.J. Kim, Two-dimensional transition metal dichalcogenides and metal oxide hybrids for gas sensing. ACS Sens. **3**(10), 2045–2060 (2018). https://doi.org/10.1021/acssensors.8b01077

3. A.S. Agnihotri, A. Varghese, M. Nidhin, Transition metal oxides in electrochemical and bio sensing: a state-of-art review. Appl. Surf. Sci. Adv. **4**, 100072 (2021). https://doi.org/10.1016/j.apsadv.2021.100072

4. Y.H. Ting, J.Y. Chen, C.W. Huang, T.K. Huang, C.Y. Hsieh et al., Observation of resistive switching behavior in crossbar core-shell Ni/NiO nanowires memristor. Small **14**(6), 1703153 (2018). https://doi.org/10.1002/smll.201703153

5. K. Nagashima, T. Yanagida, K. Oka, M. Taniguchi, T. Kawai et al., Resistive switching multistate nonvolatile memory effects in a single cobalt oxide nanowire. Nano Lett. **10**(4), 1359–1363 (2010). https://doi.org/10.1021/nl9042906

6. J. Jiang, Y. Li, J. Liu, X. Huang, C. Yuan et al., Recent advances in metal oxide-based electrode architecture design for electrochemical energy storage. Adv. Mater. **24**(38), 5166–5180 (2012). https://doi.org/10.1002/adma.201202146

7. I.A. Kuznetsov, M.J. Greenfield, Y.U. Mehta, W. Merchan-Merchan, G. Salkar et al., Increasing the solar cell power output by coating with transition metal-oxide nanorods. Appl. Energy **88**(11), 4218–4221 (2011). https://doi.org/10.1016/j.apenergy.2011.04.033

8. B.K. Meyer, A. Polity, D. Reppin, M. Becker, P. Hering et al., Binary copper oxide semiconductors: from materials towards devices. Phys. Status Solidi B **249**(8), 1487–1509 (2012). https://doi.org/10.1002/pssb.201248128

9. M.A. Rafea, N. Roushdy, Determination of the optical band gap for amorphous and nanocrystalline copper oxide thin films prepared by silar technique. J. Phys. D-Appl. Phys. **42**(1), 015413 (2009). https://doi.org/10.1088/0022-3727/42/1/015413

10. L. Liao, Z. Zhang, B. Yan, Z. Zheng, Q.L. Bao et al., Multifunctional CuO nanowire devices: P-type field effect transistors and CO gas sensors. Nanotechnology **20**(8), 085203 (2009). https://doi.org/10.1088/0957-4484/20/8/085203

11. R. Khan, R. Ahmad, P. Rai, L.W. Jang, J.H. Yun et al., Glucose-assisted synthesis of $Cu_2O$ shuriken-like nanostructures and their application as nonenzymatic glucose biosensors. Sens. Actuators B Chem. **203**, 471–476 (2014). https://doi.org/10.1016/j.snb.2014.06.128

12. A. Li, H.H. Song, W.B. Wan, J.S. Zhou, X.H. Chen, Copper oxide nanowire arrays synthesized by in-situ thermal oxidation as an anode material for lithium-ion batteries. Electrochim. Acta **132**, 42–48 (2014). https://doi.org/10.1016/j.electacta.2014.03.123

13. A. Bhaumik, A. Haque, P. Karnati, M.F.N. Taufique, R. Patel et al., Copper oxide based nanostructures for improved solar cell efficiency. Thin Solid Films **572**, 126–133 (2014). https://doi.org/10.1016/j.tsf.2014.09.056

14. M. Le, M. Ren, Z. Zhang, P.T. Sprunger, R.L. Kurtz et al., Electrochemical reduction of $CO_2$ to $CH_3OH$ at copper oxide surfaces. J. Electrochem. Soc. **158**(5), E45–E49 (2011). https://doi.org/10.1149/1.3561636

15. Z.P. Zhu, Z.Y. Liu, S.J. Liu, H.X. Niu, T.D. Hu et al., No reduction with $NH_3$ over an activated carbon-supported copper oxide catalysts at low temperatures. Appl. Catal. B Environ. **26**(1), 25–35 (2000). https://doi.org/10.1016/S0926-3373(99)00144-7

16. M. Hara, T. Kondo, M. Komoda, S. Ikeda, K. Shinohara et al., $Cu_2O$ as a photocatalyst for overall water splitting under visible light irradiation. Chem. Commun. **3**, 357–358 (1998). https://doi.org/10.1039/a707440i

17. R. Kas, R. Kortlever, A. Milbrat, M.T. Koper, G. Mul et al., Electrochemical $CO_2$ reduction on $Cu_2O$-derived copper nanoparticles: controlling the catalytic selectivity of hydrocarbons.

18. Phys. Chem. Chem. Phys. **16**(24), 12194–12201 (2014). https://doi.org/10.1039/c4cp01520g

19. M.E. Grigore, E.R. Biscu, A.M. Holban, M.C. Gestal, A.M. Grumezescu, Methods of synthesis, properties and biomedical applications of cuo nanoparticles. Pharmaceuticals **9**(4), 75 (2016). https://doi.org/10.3390/ph9040075

19. S.A. Akintelu, A.S. Folorunso, F.A. Folorunso, A.K. Oyebamiji, Green synthesis of copper oxide nanoparticles for biomedical application and environmental remediation. Heliyon **6**(7), e04508 (2020). https://doi.org/10.1016/j.heliyon.2020.e04508

20. S.M. Bergin, Y.H. Chen, A.R. Rathmell, P. Charbonneau, Z.Y. Li et al., The effect of nanowire length and diameter on the properties of transparent, conducting nanowire films. Nanoscale **4**(6), 1996–2004 (2012). https://doi.org/10.1039/c2nr30126a

21. N.N. Jason, W. Shen, W. Cheng, Copper nanowires as conductive ink for low-cost draw-on electronics. ACS Appl. Mater. Interfaces **7**(30), 16760–16766 (2015). https://doi.org/10.1021/acsami.5b04522

22. J. Shin, B. Jeong, J. Kim, V.B. Nam, Y. Yoon et al., Sensitive wearable temperature sensor with seamless monolithic integration. Adv. Mater. **32**(2), e1905527 (2020). https://doi.org/10.1002/adma.201905527

23. S. Han, S. Hong, J. Yeo, D. Kim, B. Kang et al., Nanorecycling: monolithic integration of copper and copper oxide nanowire network electrode through selective reversible photothermochemical reduction. Adv. Mater. **27**(41), 6397–6403 (2015). https://doi.org/10.1002/adma.201503244

24. H. Kwon, J. Kim, K. Ko, M.J. Matthews, J. Suh et al., Laser-induced digital oxidation for copper-based flexible photodetectors. Appl. Surf. Sci. **540**, 148333 (2021). https://doi.org/10.1016/j.apsusc.2020.148333

25. S. Back, B. Kang, Low-cost optical fabrication of flexible copper electrode via laser-induced reductive sintering and adhesive transfer. Opt. Laser Eng. **101**, 78–84 (2018). https://doi.org/10.1016/j.optlaseng.2017.09.027

26. H. Du, T. Wan, B. Qu, F. Cao, Q. Lin et al., Engineering silver nanowire networks: from transparent electrodes to resistive switching devices. ACS Appl. Mater. Interfaces **9**(24), 20762–20770 (2017). https://doi.org/10.1021/acsami.7b04839

27. D.J. Joe, S. Kim, J.H. Park, D.Y. Park, H.E. Lee et al., Laser-material interactions for flexible applications. Adv. Mater. **29**(26), 1606586 (2017). https://doi.org/10.1002/adma.201606586

28. J.H. Shin, J.H. Park, J. Seo, T.H. Im, J.C. Kim et al., A flash-induced robust Cu electrode on glass substrates and its application for thin-film muleds. Adv. Mater. **33**(13), e2007186 (2021). https://doi.org/10.1002/adma.202007186

29. C. Zhang, Y. Xie, H. Deng, T. Tumlin, C. Zhang et al., Monolithic and flexible $ZnS/SnO_2$ ultraviolet photodetectors with lateral graphene electrodes. Small **13**(18), 1604197 (2017). https://doi.org/10.1002/smll.201604197

30. G. Kresse, J. Furthmuller, Efficiency of ab-initio total energy calculations for metals and semiconductors using a plane-wave basis set. Comput. Mater. Sci. **6**(1), 15–50 (1996). https://doi.org/10.1016/0927-0256(96)00008-0

31. G. Kresse, J. Furthmuller, Efficient iterative schemes for ab initio total-energy calculations using a plane-wave basis set. Phys. Rev. B **54**(16), 11169–11186 (1996). https://doi.org/10.1103/physrevb.54.11169

32. G. Kresse, D. Joubert, From ultrasoft pseudopotentials to the projector augmented-wave method. Phys. Rev. B **59**(3), 1758–1775 (1999). https://doi.org/10.1103/PhysRevB.59.1758

33. P.E. Blochl, Projector augmented-wave method. Phys. Rev. B **50**(24), 17953–17979 (1994). https://doi.org/10.1103/physrevb.50.17953

34. J.P. Perdew, K. Burke, M. Ernzerhof, Generalized gradient approximation made simple. Phys. Rev. Lett. **77**(18), 3865–3868 (1996). https://doi.org/10.1103/PhysRevLett.77.3865

35. S. Smidstrup, A. Pedersen, K. Stokbro, H. Jonsson, Improved initial guess for minimum energy path calculations. J. Chem. Phys. **140**(21), 214106 (2014). https://doi.org/10.1063/1.4878664

36. D. Sheppard, R. Terrell, G. Henkelman, Optimization methods for finding minimum energy paths. J. Chem. Phys. **128**(13), 134106 (2008). https://doi.org/10.1063/1.2841941

37. N. Ashburn, Y. Zheng, S. Thampy, S. Dillon, Y.J. Chabal et al., Integrated experimental-theoretical approach to determine reliable molecular reaction mechanisms on transition-metal oxide surfaces. ACS Appl. Mater. Interfaces **11**(33), 30460–30469 (2019). https://doi.org/10.1021/acsami.9b09700

38. F. Fievet, J. Lagier, B. Blin, B. Beaudoin, M. Figlarz, Homogeneous and heterogeneous nucleations in the polyol process for the preparation of micron and submicron size metal particles. Solid State Ion. **32–33**, 198–205 (1989). https://doi.org/10.1016/0167-2738(89)90222-1

39. J.H. Park, S. Han, D. Kim, B.K. You, D.J. Joe et al., Plasmonic-tuned flash Cu nanowelding with ultrafast photochemical-reducing and interlocking on flexible plastics. Adv. Funct. Mater. **27**(29), 1701138 (2017). https://doi.org/10.1002/adfm.201701138

40. H. Amekura, O.A. Plaksin, K. Kono, Y. Takeda, N. Kishimoto, Production of $Cu_2O$ nanoparticles in $SiO_2$ by ion implantation and two-step annealing at different oxygen pressures. J. Phys. D-Appl. Phys. **39**(16), 3659–3664 (2006). https://doi.org/10.1088/0022-3727/39/16/020

41. L.L.S. Valladares, D.H. Salinas, A.B. Dominguez, D.A. Najarro, S.I. Khondaker et al., Crystallization and electrical resistivity of $Cu_2O$ and CuO obtained by thermal oxidation of cu thin films on $SiO_2$/Si substrates. Thin Solid Films **520**(20), 6368–6374 (2012). https://doi.org/10.1016/j.tsf.2012.06.043

42. M.Z. Su, J. Cao, X. Tian, Y.L. Zhang, H.B. Zhao, Mechanism and kinetics of $Cu_2O$ oxidation in chemical looping with oxygen uncoupling. Proc. Combust. Inst. **37**(4), 4371–4378 (2019). https://doi.org/10.1016/j.proci.2018.06.162

43. D. Kim, J. Kwon, J. Jung, K. Kim, H. Lee et al., A transparent and flexible capacitive-force touch pad from high-aspect-ratio copper nanowires with enhanced oxidation resistance for applications in wearable electronics. Small Methods **2**(7), 1800077 (2018). https://doi.org/10.1002/smtd.201800077

44. D. Kim, J. Bang, P. Won, Y. Kim, J. Jung et al., Biocompatible cost-effective electrophysiological monitoring with oxidation-free Cu–Au core–shell nanowire. Adv. Mater. Technol. **5**(12), 2000661 (2020). https://doi.org/10.1002/admt.202000661

45. J. Pak, I. Lee, K. Cho, J.K. Kim, H. Jeong et al., Intrinsic opto-electronic characteristics of $MoS_2$ phototransistors via a fully transparent van der Waals heterostructure. ACS Nano **13**(8), 9638–9646 (2019). https://doi.org/10.1021/acsnano.9b04829